Detection of *Xylella fastidiosa* infection symptoms with airborne multispectral and thermal imagery: assessing bandset reduction performance from hyperspectral analysis

Poblete[1], T., Camino[2], C., Beck[2], P.S.A., Hornero[3], A., Kattenborn[4], T., Saponari[5], M., Boscia[5], D., Navas-Cortés[6], J.A., Zarco-Tejada[1,7,6], P.J.

[1] School of Agriculture and Food, Faculty of Veterinary and Agricultural Sciences (FVAS), University of Melbourne, Melbourne, Victoria, Australia

[2] European Commission (EC), Joint Research Centre (JRC), Directorate D-Sustainable Resources, Via E. Fermi 2749 – TP 261, 26a/043, I-21027 Ispra (VA), Italy

[3] Department of Geography, Swansea University, SA2 8PP Swansea, United Kingdom

[4] Institute of Geography and Geoecology (IFGG), Karlsruhe Institute of Technology (KIT), Karlsruhe, Germany.

[5] CNR, Istituto per la Protezione Sostenibile delle Piante (IPSP), via Amendola, 122/D - I-70126, Bari, Italy

[6] Instituto de Agricultura Sostenible (IAS), Consejo Superior de Investigaciones Científicas (CSIC), Avenida Menéndez Pidal s/n, 14004 Córdoba, Spain

[7] Department of Infrastructure Engineering, Melbourne School of Engineering (MSE), University of Melbourne, Melbourne, Victoria, Australia

Submitted to ISPRS Journal of Photogrammetry and Remote Sensing

October 2019
Revised February 2020

Abstract

Xylella fastidiosa (*Xf*) is a harmful plant pathogenic bacterium, able to infect over 500 plant species worldwide. Successful eradication and containment strategies for harmful pathogens require large-scale monitoring techniques for the detection of infected hosts, even when they do not display visual symptoms. Although a previous study using airborne hyperspectral and thermal imagery has shown promising results for the early detection of *Xf*-infected olive (*Olea europaea*) trees, further work is needed when adopting these techniques for large scale monitoring using multispectral cameras on board airborne platforms and satellites. We used hyperspectral and thermal imagery collected during a two-year airborne campaign in a *Xf*-infected area in southern Italy to assess the performance of spectrally constrained machine-learning algorithms for this task. The algorithms were used to assess multispectral bandsets, selected from the original hyperspectral imagery, that were compatible with large-scale monitoring from unmanned platforms and manned aircraft. In addition, the contribution of solar-induced chlorophyll fluorescence (SIF) and the temperature-based Crop Water Stress Index (CWSI) retrieved from hyperspectral and thermal imaging, respectively, were evaluated to quantify their relative importance in the algorithms used to detect *Xf* infection. The detection performance using support vector machine algorithms decreased from ~80% (kappa, $\kappa = 0.42$) when using the original full hyperspectral dataset including SIF and CWSI to ~74% ($\kappa = 0.36$) when the optimal set of six spectral bands most sensitive to *Xf* infection were used in addition to the CWSI thermal indicator. When neither SIF nor CWSI were used, the detection yielded less than 70% accuracy (decreasing κ to very low performance, 0.29), revealing that tree temperature was more important than chlorophyll fluorescence for the *Xf* detection. This work demonstrates that large-scale *Xf* monitoring can be supported using

airborne platforms carrying multispectral and thermal cameras with a limited number of spectral bands (e.g., six to 12 bands with 10 nm bandwidths) as long as they are carefully selected by their sensitivity to the *Xf* symptoms. More precisely, the blue (bands between 400 and 450 nm to derive the NPQI index) and thermal (to derive CWSI from tree temperature) were the most critical spectral regions for their sensitivity to *Xf* symptoms in olive.

Keywords: hyperspectral, multispectral, thermal, radiative transfer, *Xylella fastidiosa*, airborne, machine learning

1. Introduction

Almost 500 plant species are susceptible to the bacterial pathogen *Xylella fastidiosa* (*Xf*), which causes major plant diseases and severe damage (EFSA, 2018). Originally from the Americas (Purcell, 1997), *Xf* is now a global threat given its discovery in Iran, Taiwan, and Europe in 2013 (Saponari *et al.*, 2016), and very recently in Israel in 2019 (EPPO, 2019). In Italy, *Xf* subsp. *pauca* is the causal agent of olive quick decline syndrome (OQDS), which has devastated ancient olive (*Olea europaea*) trees as well as large commercial orchards, leading to severe economic and societal damage (Almeida, 2016). Outbreaks associated with different *Xf* strains have been detected in northern Italy, France, the Balearic Islands, mainland Spain, and Portugal (EFSA, 2018; EPPO, 2019). The current eradication and containment strategies for *Xf* require large-scale monitoring tools for the early detection of infected plants (Almeida, 2016), a task traditionally accomplished by visual field surveys followed by laboratory analyses. To make this monitoring more effective, efforts towards detecting the pre-visual stages of infection using remote sensing are critical (Zarco-Tejada *et al.*, 2018), as they could be used to prevent infected but asymptomatic trees from contributing to *Xf* epidemics (Saponari *et al.*, 2016).

Recent work in the context of the Italian *Xf* outbreak utilized two years of high-resolution hyperspectral and thermal imagery to evaluate more than 7,000 olive trees in the field, revealing that the pre-visual detection of *Xf*-infected trees was feasible using radiative transfer modeling and spectral plant-trait retrievals from imaging spectroscopy and thermal data (Zarco-Tejada *et al.*, 2018). This study showed that the changes in specific plant functional traits detected using hyperspectral and thermal imagery revealed an *Xf* infection months before symptoms were visible to the naked eye. In particular, i) the NPQI index

(Barnes *et al.*, 1992), calculated in the blue region (400-450 nm) and hypothesized to be sensitive to the chlorophyll degradation into phaeophytine (Peñuelas *et al.*, 1995), ii) the Crop Water Stress Index (CWSI) calculated from top of the canopy tree crown temperature, anthocyanins and carotenoid pigment content, and the iii) solar induced fluorescence, were the spectral plant trait indicators that contributed the most in the detection of the *Xf*-induced infection symptoms. Moreover, the importance of the spectral indicators varied as a function of the disease severity, showing that NPQI and CWSI were critical in the separation between asymptomatic and symptomatic trees, but their relative importance decreased once the disease reached more advanced stages. Once the trees were symptomatic, fluorescence became the most sensitive indicator to detect the severity of *Xf* symptoms.

In that study, the accuracy of detecting symptomatic trees exceeded 80% (kappa coefficient, $\kappa = 0.61$), as confirmed using field validation data comprising visual evaluations and qPCR laboratory assessments. Important inputs for the detection of *Xf* included spectral ratios in the blue wavelengths, plant traits such as tree temperature, anthocyanin and carotenoid pigment content estimated using a model inversion, and estimates of solar-induced chlorophyll fluorescence. Given the difficulty of visually tracking such early manifestations of infection, remote sensing to detect early *Xf* infection was more accurate than a visual inspection by plant pathologists. Advanced remote sensing methods therefore proved useful for tackling the major challenges in plant disease detection based on the early identification of non-visual symptoms. This early detection is expected to be critical for the eradication or containment of devastating plant diseases, such as *Xf* worldwide.

Although hyperspectral cameras are becoming increasingly miniaturized, with several reports of successful monitoring of physiological traits achieved using micro- and nano-hyperspectral imaging technology onboard drones (Zarco-Tejada *et al.*, 2012; Aasen *et al.*, 2018), the limitations of platform endurance and regulatory restrictions that require line-of-sight flying prevent their operational use in large-scale contexts. Most commercially available unmanned aerial systems (UAS) can cover less than 100 ha when carrying hyperspectral imagers due to the payload capacity and the requirements for carrying linear-array imaging spectrometers on a solar plane, which in most cases reduces the efficiency of the flights. Nevertheless, drones would allow the frequent monitoring of smaller areas in a cost-efficient manner, which is essential when monitoring disease outbreaks.

In the particular case of hyperspectral imagery collected from individual orchard trees, a pixel size of 40–50 cm is required, further reducing the flight efficiency (Aasen et al., 2018; Zarco-Tejada *et al.*, 2012). In the case of *Xf*, one of the areas under intense monitoring is in Apulia, Italy, which currently extends 715,000 ha (Saponari *et al.*, 2018). Over such a large scale, monitoring projects with a clear requirement for ensuring high spatial resolution acquisitions from both hyperspectral and thermal imaging systems have the additional limitation of producing a vast amount of data, generally requiring a long processing time. For the case of both UAS and manned aircraft platforms, existing multispectral cameras are more cost efficient and easier to operate than most hyperspectral sensors, providing higher spatial resolutions and a much faster processing turn-around. However, they offer only a limited number of narrow spectral bands (typically between five and 12 bands when two or more cameras are coupled in tandem). Reducing the spectral information limits our ability to accurately determine the canopy properties, as the vegetation spectrum is a complex product

shaped by plant traits including both crown features and leaf components, which affect partly overlapping wavelength regions (Ollinger, 2011, Kattenborn *et al*., 2017). Accordingly, the success of both empirical approaches (e.g., machine learning) and process-based approaches (e.g., the inversion of radiative transfer models) often greatly depends on the spectral information available (Blackburn, 2006, Homolova *et al*., 2013, Houbourg *et al*., 2015). Plant traits describing canopy structure and leaf biochemistry have been successfully retrieved from hyperspectral data through the inversion of radiative transfer models. This has been achieved using well-established models, such as the PROSPECT leaf model (Jacquemoud and Baret, 1990) or the newer version PROSPECT-D (Feret *et al.,* 2017), coupled with homogeneous approximations of canopies, such as SAIL (Verhoef *et al.,* 1984) or, for more complex canopy representations, 3-D simulations such as FLIGHT (North, 1996) and DART (Gastellu-Etchegorry *et al.,* 1996, 2004), among others. Due to the complexity of the radiative transfer in plant canopies and the corresponding complexity of physical models, the actual retrieval of leaf and canopy parameters requires modeling strategies to avoid the '*ill-posed*' problem, i.e., the risk that multiple parameter combinations lead to the same model outputs (Combal *et al*., 2003; Darvishzadeh *et al*., 2008; Jacquemoud *et al*., 2009; Li *et al*., 2011). In all cases, the use of a high number of spectral bands is a prerequisite for reducing the ill-posed problem and accurately characterizing the leaf and canopy optical properties to determine the leaf biochemistry and canopy structural traits.

When a limited number of spectral bands are available, as in common five- or six-band commercial cameras, typical approaches for vegetation characterization are based on spectral indices (as shown in Berni *et al.,* 2009; and Suarez *et al.,* 2009). Given that the bands are set to specific wavelengths, such indices enable the estimation of structural vegetation traits,

such as leaf area index (LAI) (e.g., through the calculation of the normalized difference vegetation index, NDVI, and other indices related to canopy structure), or leaf constituents, such as the chlorophyll content (through the chlorophyll absorption reflectance index, CARI, and the transformed chlorophyll absorption reflectance index, TCARI family of indices and the red edge ratios). Although these bandsets are very limited in terms of their spectral capacity for estimating different photosynthetic pigments, several groups have demonstrated the successful assessment of stress in different crops using unmanned systems (Berni *et al.*, 2009; Suarez *et al.*, 2009) and manned aircraft (Sepulcre-Canto *et al.*, 2006). In fact, lower-cost cameras are capable of detecting subtle spectral changes resulting from xanthophyll pigment dynamics and chlorophyll content reductions, and were successfully used in the first attempt to retrieve fluorescence emission data from vegetation with 1-nm full-width half-maximum (FWHM) filters as a proxy for stress (Zarco-Tejada *et al.*, 2009). Due to the demonstrated capabilities of these multispectral cameras for the retrieval of plant traits, their use for the large-scale monitoring of harmful organisms is plausible and opens several avenues for the operational assessment of large areas using manned aircraft. Nevertheless, the expected reduction in performance caused by the limited spectral information used and the impact on the retrieval of plant-trait data required for the pre-visual detection of harmful pathogens should be quantified before their use in large-scale disease-monitoring applications.

Here, we assessed the potential of using multispectral bandsets in the context of unmanned and manned remote sensing for large-scale monitoring of *Xf* infection. We used a two-year hyperspectral dataset acquired from a *Xf*-infected area in southern Italy in 2016 and 2017 as a benchmark. Field measurements of physiological traits and leaf reflectance were evaluated

to assess the consistency of the spectral changes observed across leaf and canopy scales as a function of the different levels of the disease severity (DS) induced by *Xf*. The specific bands, spectral indices, and contributions of the thermal and solar-induced chlorophyll fluorescence traits were also evaluated in the machine-learning models.

2. Material and Methods

2.1. Study area and field data collection

The study area was located within the *Xylella fastidiosa* (*Xf*)-infected zone in Apulia, southern Italy (Figure 1a). Field and airborne data were collected as part of an international research collaboration funded by the POnTE and XF-ACTORS projects (details of the datasets used can be found in Zarco-Tejada *et al.*, 2018). A total of 15 olive (*Olea europaea*) orchards in the *Xf*-infected area were selected, and the DS of 3,324 trees was evaluated in June 2016, with a further 3,972 trees evaluated in July 2017. The evaluations consisted of a visual inspection of every tree by a team of plant pathologists, who scored their DS levels on a 0–4 scale based on the percentage of the crown showing disease symptoms; 0 was assigned to asymptomatic trees, and 4 to trees with a high number of dead branches. The olive orchards studied contained old trees (> 50 years) most of them of local cultivars such as Cellina di Nardò and Ogliarola Salentina. In 2016, 1,438 asymptomatic trees (DS = 0) were identified, and 1,886 symptomatic trees were also included in the study (762, DS = 1; 802, DS = 2; 250, DS = 3; and 72, DS = 4). In 2017, a total of 2,607 asymptomatic (DS = 0) and 1,365 symptomatic trees (686, DS = 1; 542, DS = 2; 122, DS = 3; and 15, DS = 4) were evaluated. Leaf physiological indicators were measured in trees with a range of DS levels, using both asymptomatic (non-symptomatic; NS) and symptomatic (S) leaves on each sampled tree.

This approach was aimed at capturing the large heterogeneity in visual symptoms observed within each symptomatic tree. The chlorophyll content, anthocyanin content index, and epidermal flavonol content of each leaf were measured using a leaf clip Dualex Scientific+ handheld instrument (Force-A, Orsay, France). The physiological measurements were carried out on 1,001 NS leaves from trees for each DS level ($NS_{DS=0}$ = 36, $NS_{DS=1}$ = 211, $NS_{DS=2}$ = 251, $NS_{DS=3}$ = 426, and $NS_{DS=4}$ = 77) and 987 S leaves ($S_{DS=1}$ = 187, $S_{DS=2}$ = 287, $S_{DS=3}$ = 447, $S_{DS=4}$ = 66). Leaf chlorophyll fluorescence (Ft) was measured in the field using a FluorPen FP1000 (Photon Systems Instruments, Brno, Czech Republic) using 2,677 leaves (1,369 NS and 1,308 S leaves) comprising 76, 281, 352, 577, and 83 samples of $NS_{DS=0}$, $NS_{DS=1}$, $NS_{DS=2}$, $NS_{DS=3}$, and $NS_{DS=4}$, respectively, and 274, 402, 554, and 78 leaves from S1, S2, S3, and S4 symptomatic trees, respectively.

Leaf reflectance spectra in the visible and near-infrared regions were measured using a PolyPen RP400 handheld spectrometer (Photon Systems Instruments) to derive spectral indices related to the leaf photosynthetic pigments. A total of 1,543 leaf-level measurements were carried out, comprising 782 measurements for asymptomatic NS and 761 for symptomatic S leaves. Among the NS leaves, a total of 65, 82, 200, 383, and 52 measurements were carried out for trees rated as DS 0, 1, 2, 3, and 4, respectively. For the symptomatic S leaves of trees rated as DS 1, 2, 3, and 4, a total of 80, 252, 356, and 73 leaf spectral measurements were made, respectively. The main rationale for carrying out leaf spectral measurements was to evaluate the consistency of the spectral effects detected across the leaf and canopy levels, in particular to assess whether the spectral changes observed in the hyperspectral images were driven by leaf processes.

2.2. Airborne campaigns using hyperspectral and thermal cameras

A VNIR linear-array hyperspectral imager (Headwall Photonics, Fitchburg, MA, USA) and a thermal camera (SC655c; FLIR Systems, Wilsonville, OR, USA) were mounted on a manned aircraft to overfly three areas totaling 1,200 ha in the *Xf*-infected zone in Apulia, southern Italy (Figure 1b) on June 28, 2016, and July 5, 2017.

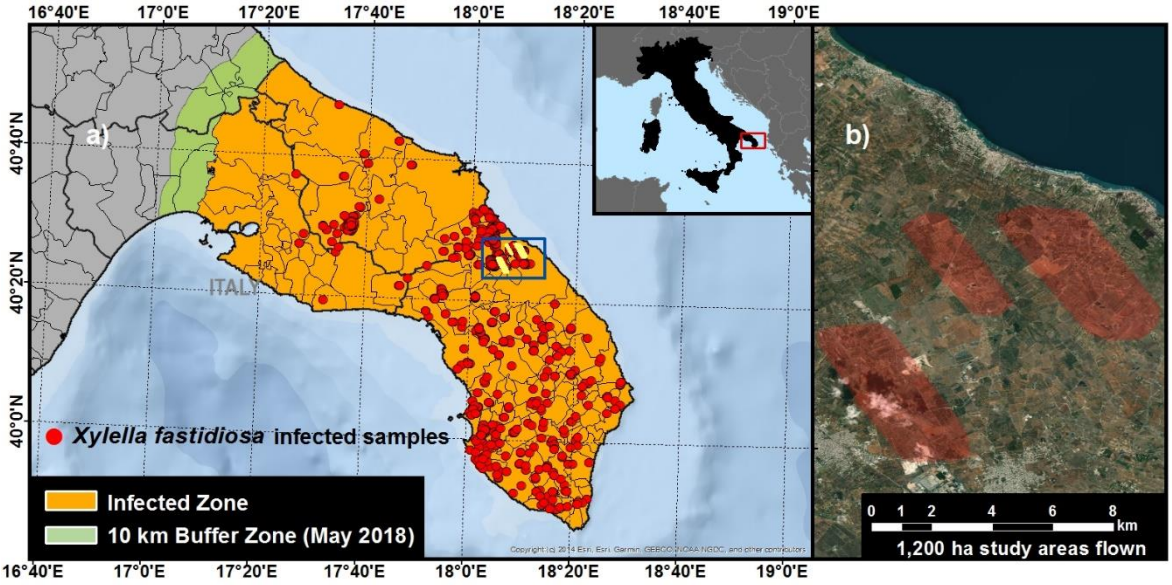

Figure 1. The *Xylella fastidiosa*-infected zone in Apulia, southern Italy. Source: 2018 SANTE GIS, updated 04 June 2018 (a), and the three study areas overflown with hyperspectral and thermal cameras as part of this study (b).

The sensors were flown on a solar plane at 500 m above ground level, yielding a 40-cm and 60-cm pixel resolution for the hyperspectral (Figure 2a) and thermal (Figure 2b) images, respectively. The hyperspectral scanner acquired images using an 8-mm focal-length lens and an instantaneous field of view (IFOV) of 0.93 mrad, yielding an angular FOV of 50°. The sensor was operated at 50 frames per second (fps) with an 18-ms integration time, collecting data in the 400–885-nm spectral region, with 260 bands at 1.85 nm/pixel and 12

bits. Using a 25-μm slit, the sensor delivered imagery with a bandwidth of 6.4 nm FWHM. The hyperspectral data were radiometrically calibrated in an optics laboratory using a CSTM-USS-2000C integrating sphere (LabSphere, North Sutton, NH, USA), which allowed the digital values to be converted into radiance levels for use later in the atmospheric correction of the imagery. Atmospheric correction was carried out using the Simple Model of Atmospheric Radiative Transfer of Sunshine (SMARTS) model (Gueymard, 1995, 2005, 2001; Gueymard *et al*., 2002), using an aerosol optical depth (AOD) measured with a Micro-Tops II sunphotometer (Solar LIGHT Co., Philadelphia, PA, USA). This approach has been used before with multispectral (Berni *et al.,* 2009) and hyperspectral data (Calderon *et al.*, 2013; 2015; Zarco-Tejada *et al.*, 2012) to obtain the surface reflectance for the quantitative assessment of vegetation stress (Zarco-Tejada *et al.,* 2018). Image orthorectification was carried out using Parametric Geocoding & Orthorectification for Airborne Optical Scanner Data (PARGE; ReSe Applications Schläpfer, Wil, Switzerland) with inputs from an inertial measuring unit (IG500 model; SBG Systems, Carrières-sur-Seine, France) attached to and synchronized with the hyperspectral sensor.

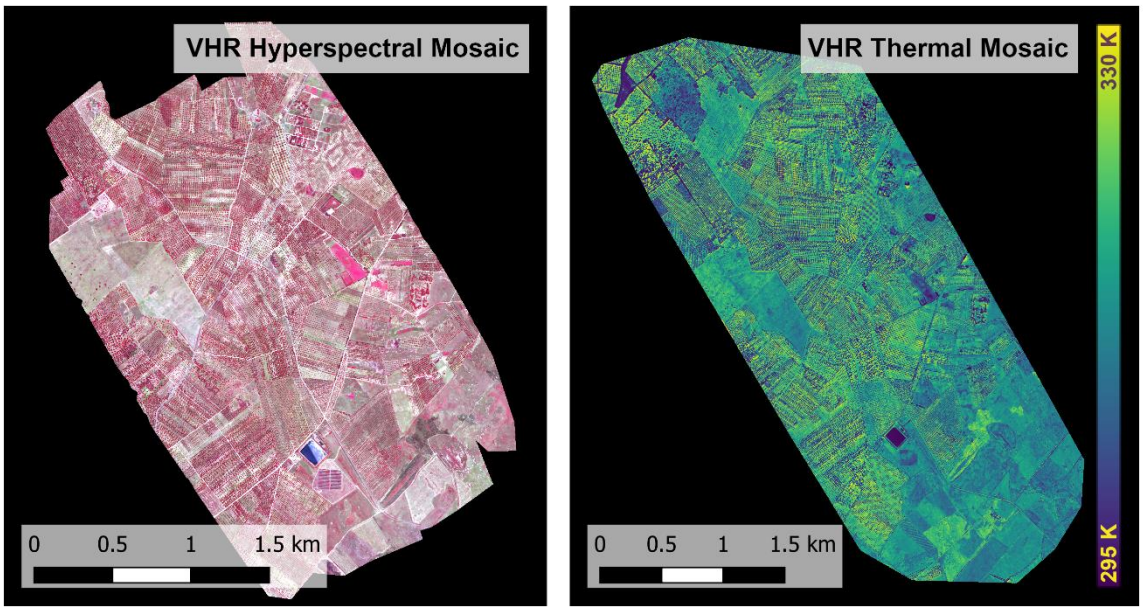

a) **b)**

Figure 2. Example hyperspectral mosaic acquired over a study site affected by *Xylella fastidiosa* using 260 spectral bands in the 400–885-nm wavelength bands, yielding a 40-cm pixel resolution (a). Thermal mosaic acquired in the 7.5–14-µm spectral region at a 60-cm resolution (b).

The FLIR SC655c thermal camera flown over the study sites covered a 7.5–14.0-µm spectral range and was operated using a 24.6-mm f/1.0 lens. Soil temperature from different locations were measured for vicarious calibrations (as described by Calderon *et al.*, 2013). Image segmentation methods were applied to the hyperspectral and thermal images to identify individual tree crowns using an automatic object-based image analysis (as described by Zarco-Tejada *et al.*, 2018). Niblack's thresholding method (Niblack, 1986) and Sauvola's binarization techniques (Sauvola and Pietikäinen, 2000) were used to separate the tree crowns from the background, removing soil effects at the border of the tree crowns and within-crown shadows. These algorithms were used to extract the mean tree-crown temperature (Figure 3) from the thermal imagery and the mean radiance and reflectance spectra (Figure 4) from the

hyperspectral imagery. This method ensures that the spectra are extracted from pure vegetation pixels, reducing the effects due to background and areas not covered by vegetation. The high spatial resolution imagery used was critical to avoid pixels of mixed scene components for this particular case of heterogeneous orchards with direct soil and background exposure.

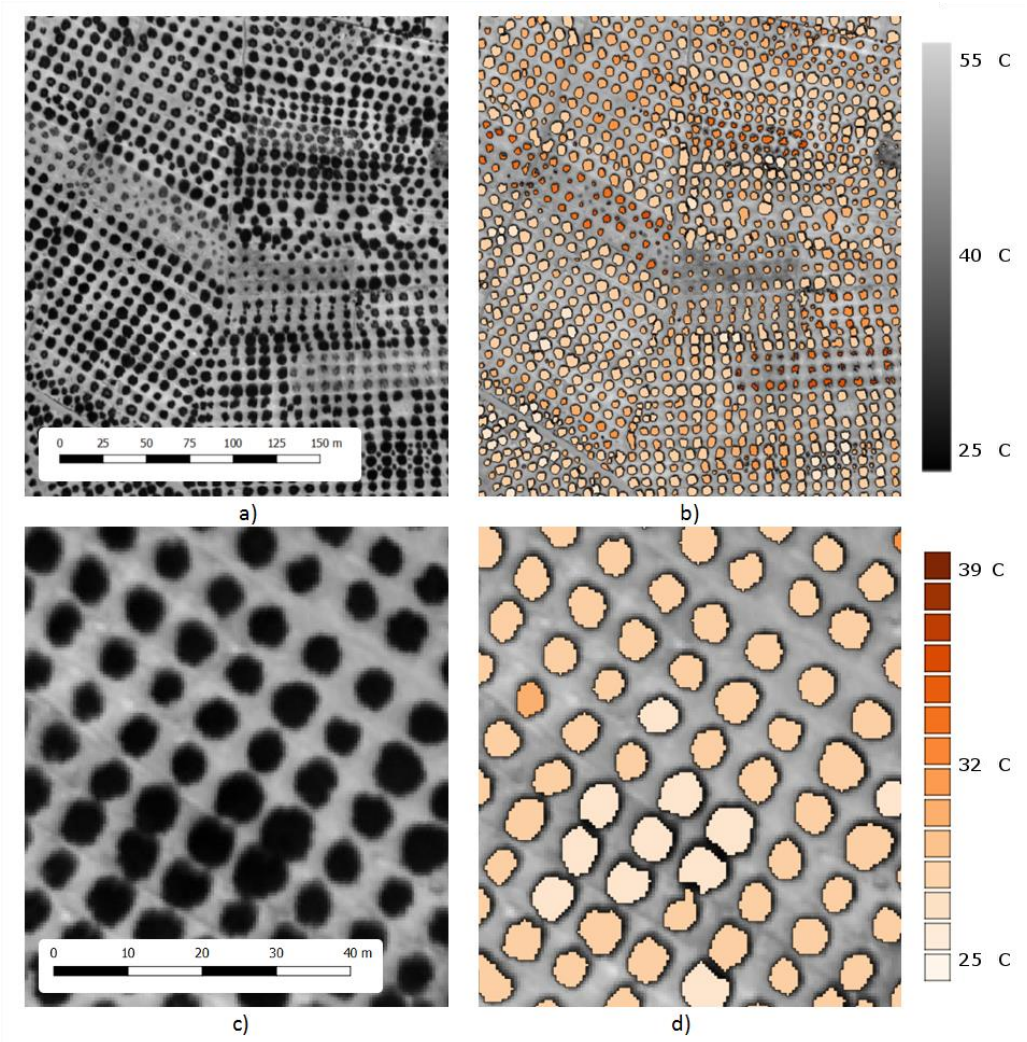

Figure 3. Example of a 60-cm-resolution thermal image (a) and the corresponding automated tree segmentation using object-based crown detection algorithms (b). Details of the VHR thermal imagery and crown identification are shown in (c) and (d), respectively.

The average tree-crown temperature was used to calculate the CWSI (Jackson *et al*., 1981), since *Xf* infection reduces transpiration (Zarco-Tejada *et al.*, 2018). The average tree-crown radiance and reflectance spectra, described in 260 spectral bands at 6.5 nm FWHM, were used to invert the radiative transfer models and calculate the narrow-band hyperspectral indices (NBHIs) related to leaf biochemistry and canopy structure. Every tree evaluated in the field was thereby identified and automatically delineated in the images (Figure 4abc), and their radiances and reflectance spectra were extracted (Figure 4d). The irradiance measured in the field at the time of the flights enabled the calculation of the solar-induced chlorophyll fluorescence using the Fraunhofer line-depth (FLD) method (Plascyk and Gabriel, 1975). Hyperspectral indices, CWSI, and SIF were calculated from each mean spectrum and tree temperature extracted for the individual tree crowns evaluated in the field.

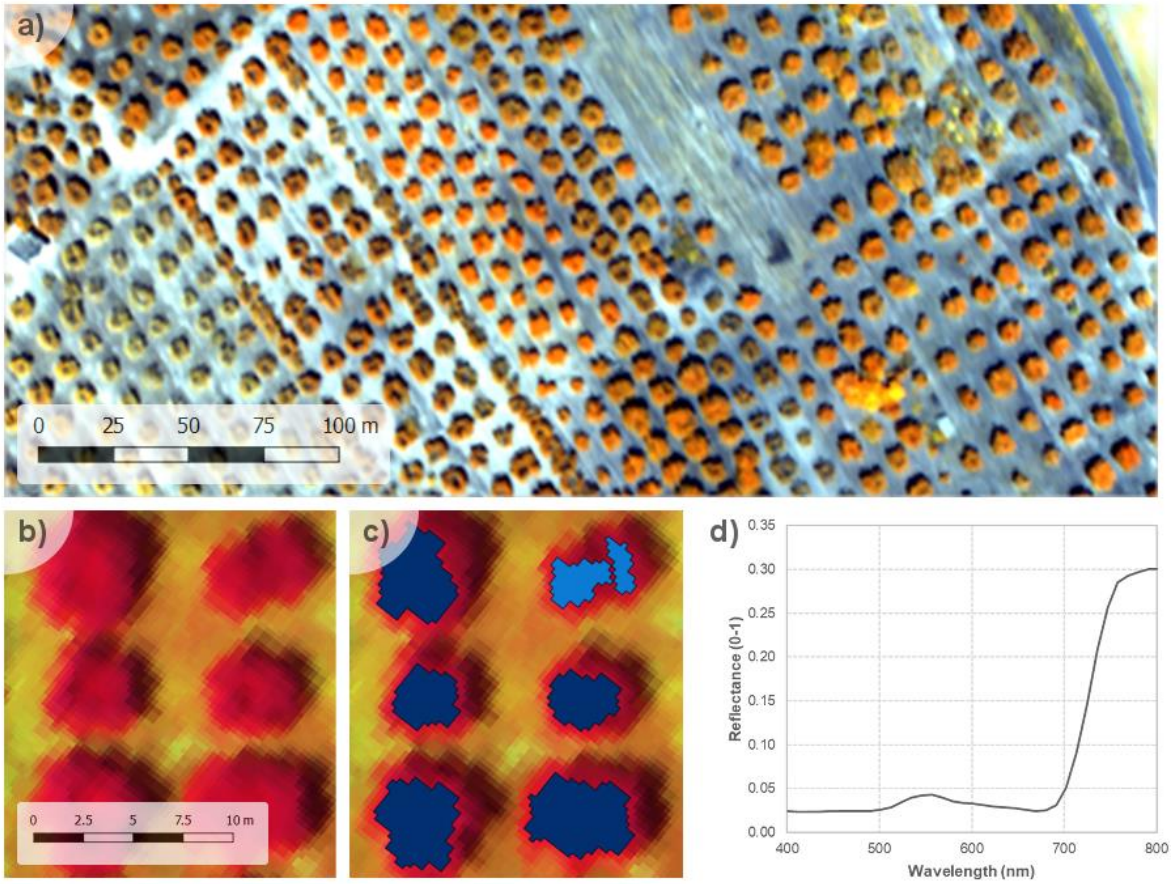

Figure 4. Example of the 40-cm-resolution hyperspectral imagery acquired using 260 spectral bands (a). Very-high-resolution hyperspectral images (b) were used for the automated tree-crown segmentation using an object-based crown detection algorithm (c) to extract the pure crown reflectance from each individual tree (d).

2.3. Modeling methods

To assess the remote detection of *Xf* symptoms from spectrally reduced datasets, seven *sources of data* (*SoD*) were considered: the original hyperspectral data used to estimate plant traits using model inversion (*SoD 1*), the calculated narrow-band hyperspectral indices, NBHIs (*SoD 2*), and the SIF calculated using the FLD method (*SoD 3*). Additionally, convoluted data from the original hyperspectral data were used to simulate multispectral bandsets of 10 nm FWHM (*SoD 4*) and to calculate the multispectral indices (MI) (*SoD 5*) and broadband indices typically acquired from color-infrared (CIR) and red-green-blue (RGB) cameras (*SoD 6*). Finally, thermal images were used to calculate CWSI (*SoD 7*).

The *SoD 1* bandset was built from the mean narrow-band hyperspectral reflectance spectrum extracted from each individual tree crown to estimate the leaf biochemical constituents and canopy structural parameters, including the chlorophyll content, carotenoid content, anthocyanin content, mesophyll structure, LAI, and the average leaf angle using a model inversion (Zarco-Tejada *et al.,* 2018; used here as benchmark dataset). The inversion method was based on the linked PROSPECT-D (Féret *et al.,* 2017) and 4SAIL (Verhoef *et al.,* 2007) models (see Supplementary Table 2 from Zarco-Tejada *et al.,* 2018 for the set of fixed and varied parameters, and their range of variation). The *SoD 2* bandset comprised the calculated NBHIs selected from the literature based on plant-trait functional groups related to chlorophyll, carotene, and xanthophyll pigments for their potential link with physiological effects caused by the *Xf* infection of the olive trees, as discussed by Zarco-Tejada *et al.* (2018). The *SoD 3* bandset comprised the SIF values calculated from the original radiance spectra using the FLD method. The *SoD 4* bandset involved convolution of the original hyperspectral data extracted from the images for each individual tree to simulate 10-nm

FWHM bandsets at the spectral resolution normally used in remote sensing cameras on board unmanned and manned aircraft systems (Jhan *et al.,* 2016). *SoD 5* was built using the convoluted data from *SoD 4* to calculate the entire set of multispectral indices. The *SoD 6* bandset used the original hyperspectral bands to simulate the CIR and RGB broadband bandsets typically acquired from airborne platforms. The blue, green, red, and near-infrared bands were convoluted at wavelengths 450, 550, 670, and 800 nm with FWHMs of 50, 100, 100, and 50 nm, respectively (Deng *et al*., 2018). Finally, *SoD 7* consisted of the CWSI calculated by normalizing the average tree-crown temperature with the air temperature and vapor pressure deficit registered at the flight time, according to the methodology proposed by Idso *et al*. (1981).

Based on previous datasets, a pool of four *sets of inputs* (*SoI*) was derived to be used by the machine-learning modeling: *SoI 1*, used here as a benchmark, included pigment-, structural-, fluorescence-, and tree temperature-based plant functional traits (PSFTs). These parameters were obtained from the plant traits estimated using a radiative transfer model inversion from the main dataset (*SoD 1*), NBHI (*SoD 2*), CWSI (*SoD 3*), and SIF (*SoD* 7). This pool of traits and indices was the most accurate for detecting *Xf*-infected trees (Zarco-Tejada *et al.,* 2018), and therefore all other models tested in this study were compared against this as a benchmark. Secondly, *SoI 2* used information from the *SoD 4* dataset, and assessed the contribution of each spectral band and spectral region in the detection of *Xf*-induced symptoms. *SoI 3* used multispectral indices from dataset *SoD 5*, which allowed the assessment of the indices most sensitive for the detection of *Xf*-induced symptoms that could be potentially measured using compact multispectral cameras. Finally, *SoI 4* used broad bands, such as blue, green, red, and near-infrared, from the *SoD 6* dataset.

As a first step, several machine-learning models were built to assess the performance of classifying asymptomatic *vs.* symptomatic trees using the benchmark set of inputs (*SoD 1*). Based on the result of this classification, the model and configuration with the best performance were selected and implemented in the next modeling steps. For the pooled sets of inputs (*SoI 2* and *SoI 3*), the input variables were sorted using a variance inflation factor (VIF) analysis, in which the VIF threshold was varied until the resulting dataset contained the least number of variables. The models using the pools of inputs (*SoI 2*, *SoI 3*, and *SoI 4*) were then built, and the improvement in the model performance in the detection of the affected trees achieved by adding SIF and CWSI data was also evaluated. Finally, an analysis of the receiving operating characteristics was performed for each model to analyze the contribution of the parameters to each model.

A total of six groups of machine-learning algorithms were built (MATLAB; Statistics and Machine Learning toolbox and Deep Learning toolbox; Mathworks Inc., Matick, MA, USA), which classified asymptomatic *vs.* symptomatic trees using the benchmark set of inputs. The groups of machine-learning algorithms were: discriminant analysis (McLachlan, 2004), decision trees (Breslow and Aha, 1997), K-nearest neighbors (KNN) (Peterson, 2009), ensemble classifiers (Galar *et al*., 2011), artificial neural networks (ANN) (Dreiseitl and Ohno-Machado, 2002), and support vector machines (SVM) (Hsu, Chang and Lin, 2003).
For all the models, 300 iterations were executed, splitting the dataset into 80% of values for use in training and 20% for use in testing. For the training process, the training data were balanced with the aim of achieving 50% asymptomatic and 50% symptomatic cases. K-fold (10-fold) cross-validation was used in the training process to avoid overfitting, and the root mean square error was used to assess the performance of each iteration. For the discriminant

analysis models, both linear and quadratic fitting functions were used to estimate the parameters for a Gaussian distribution that better described each class (symptomatic *vs*. asymptomatic).

Decision-tree algorithms were trained considering a maximum of four, 20, and 100 splits, and in all cases Gini's diversity index, towing rule, and cross-entropy were used as split criteria. Several KNN models were built combining different distance estimators (Euclidean, cosine, and cubic Monkowski) and different numbers of neighbors to be found (one, 10, and 100), while adding various weight functions to the valuing process. In the case of the ensemble classifiers, different machine-learning algorithms were integrated. First, decision trees using a maximum of 20 splits were enhanced using the Adaboost and RUSBoost boosting functions (using 30 cycles for each algorithm). Second, bootstrap aggregating trees, based on random forest trees (Breiman, 2001), were 'bagged' into different decision trees and combined into an integrated classifier. Finally, subspace discriminant and subspace KNN models were used, in which the data were randomly divided into subspaces, after which each subspace was modeled using a 10-nearest neighbor analysis or a quadratic discriminant analysis, respectively.

The ANN models were built using a double-layer feedforward artificial neural network. The input layer included the hyperspectral and thermal inputs connected using a hidden layer of five and 10 sigmoid-based function neurons, with the asymptomatic and symptomatic classes as outputs. To train the artificial neural network models, 13 different training algorithms were assessed by dividing the training dataset into 80% of values for modeling and 20% for validation. For the most accurate ANN obtained, the remaining 20% of the dataset was used

for testing. Finally, several SVM algorithms were also built using linear, quadratic, cubic, and Gaussian (radial basis function) kernels for modeling. A heuristic procedure was used to select the best kernel scale (number of subsamples) to divide all the predictor parameters.

3. Results and Discussion

The leaf fluorescence measurements consistently showed higher Ft values for asymptomatic NS leaves than for symptomatic S leaves, regardless of the disease severity DS level of the tree as a whole (Figure 6). NS leaves from symptomatic trees (DS > 0) showed Ft values approximately twice those observed in the S leaves (*p*-value < 0.001), confirming that chlorophyll fluorescence measured at the leaf level was sufficient for separating disease levels even at early infection stages (such as DS = 1).

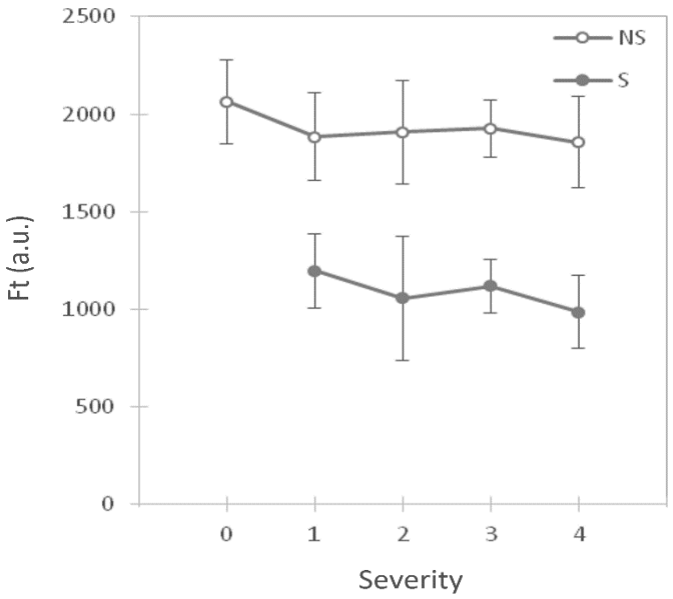

Figure 6. Fluorescence (Ft) of asymptomatic (NS) and symptomatic (S) leaves sampled from trees with different disease severity levels (0 to 4). Error bars represent the standard error. NS and S values were statistically significantly different at all severities (p<0.001).

The leaf reflectance spectra of *Xf*-infected trees with different DS levels (Figure 7a) differed consistently in the blue region, particularly in the 400- and 450-nm wavelengths, with the reflectance of the NS leaves increasing with the DS level (Figure 7b). Leaf reflectance did not vary consistently as a function of the DS level for the green, red, and near-infrared regions, however. Reflectance in the green region was the lowest for asymptomatic (NS) leaves, as expected, but did not show consistent variation at the intermediate DS levels (Figure 7c).

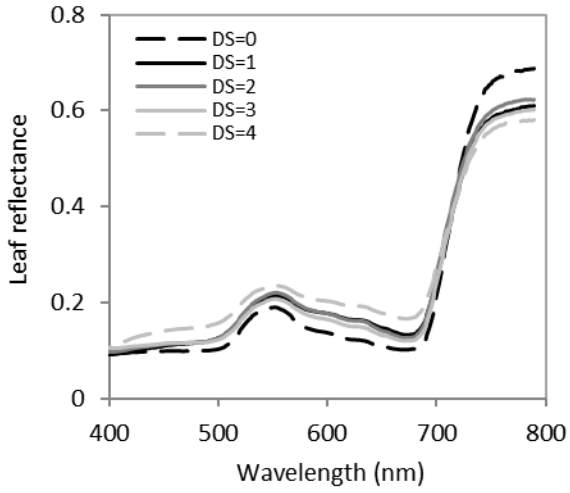

a)

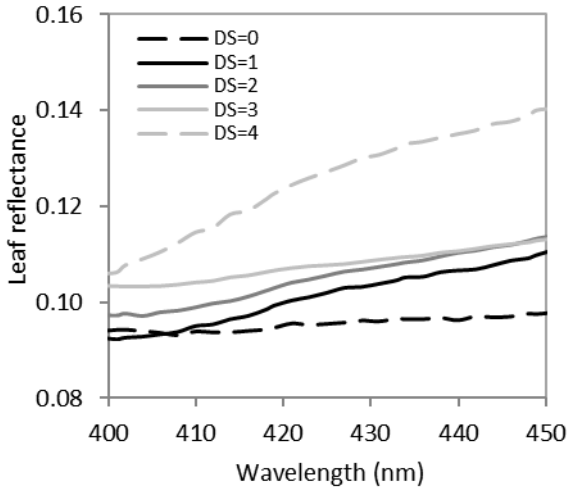

b)

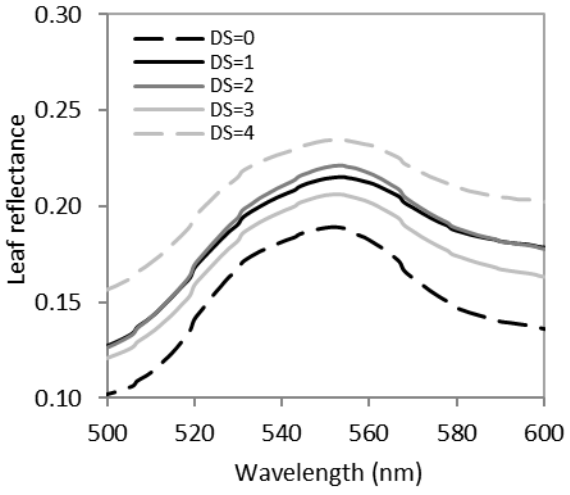

c)

Figure 7. Leaf reflectance measurements obtained from asymptomatic (DS = 0) and from *Xf*-symptomatic trees (DS > 0) showing the visible and near-infrared (400–800 nm) (a), blue (b), and green spectral regions (c).

As a result, the indices calculated from the leaf spectra from both the S and NS leaves for each DS level (Figure 8) showed generally consistent trends for green indices such as the photochemical reflectance index (PRI) (Gamon, Penuelas and Field, 1992), and red edge indices such as VOG2 (Vogelmann *et al,* 1993), chlorophyll index, CI (Zarco-Tejada *et al.*, 2001), and TCARI (Haboudane *et al*., 2002). The analysis revealed that indices such as PRI, VOG2, and CI displayed different trends for NS and S leaves. With the exception of trees with a DS score of 4, the trends for the NS leaves were consistent, showing a uniform decrease (PRI and VOG2) or increase (CI) as the DS level increased.

Indices calculated from the leaf reflectance data correlated reasonably well with the chlorophyll *a*+*b* (Cab) and anthocyanins (Anth) measurements from the same trees (Figure 9), with $r^2 = 0.53$ ($p < 0.001$) for VOG2 *vs*. Cab (Figure 9a) and $r^2 = 0.39$ ($p < 0.001$) for CTR1 *vs.* Anth (Figure 9b).

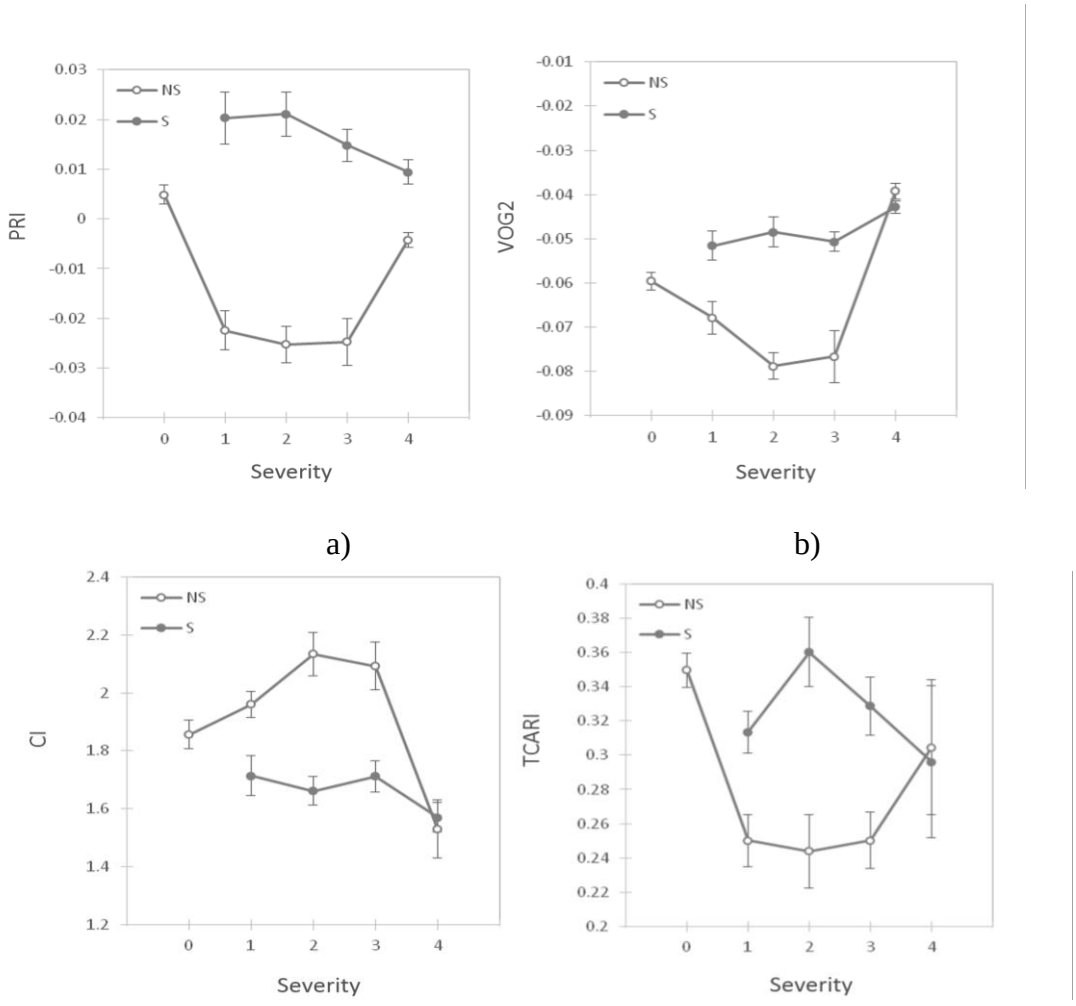

a) b)

c) d)

Figure 8. Reflectance indices calculated from asymptomatic (NS) and symptomatic (S) leaves sampled from trees with various levels of disease severity (DS 0 to 4). (a) PRI. (b) VOG2. (c) CI. (d) TCARI. The error bars represent the standard error. NS and S values were statistically significantly different ($p<0.001$) for all severities except at DS=4 for (b), (c) and (d).

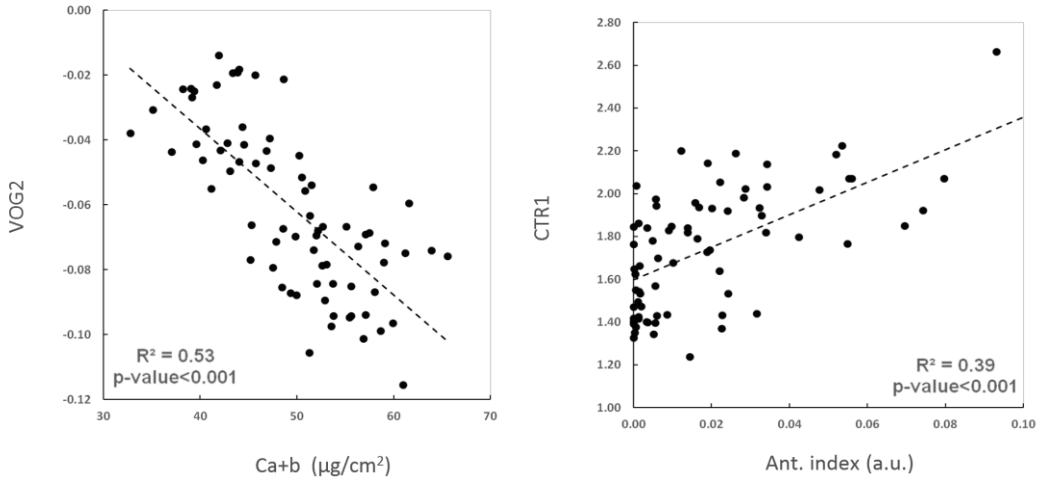

a) b)

Figure 9. Relationship between the VOG2 and CTR1 indices calculated from the leaf reflectance in the *Xf*-symptomatic leaves and the chlorophyll (a) and anthocyanin (b) contents.

The crown-level reflectance of the *Xf*-affected trees (Figure 10) followed the DS levels. This was particularly true for the blue spectral region (Figure 10a), in which the asymptomatic trees showed a lower reflectance than the trees with early or advanced disease symptoms. This result was consistent with the reflectance spectra measured at the leaf level (Figure 7b). In the remaining spectral range (above 500 nm), the signatures in the green (Figure 10b) and red regions (Figure 10c) showed more mixed patterns. The tree crowns with greater DS levels reflected more near-infrared light (Figure 10d).

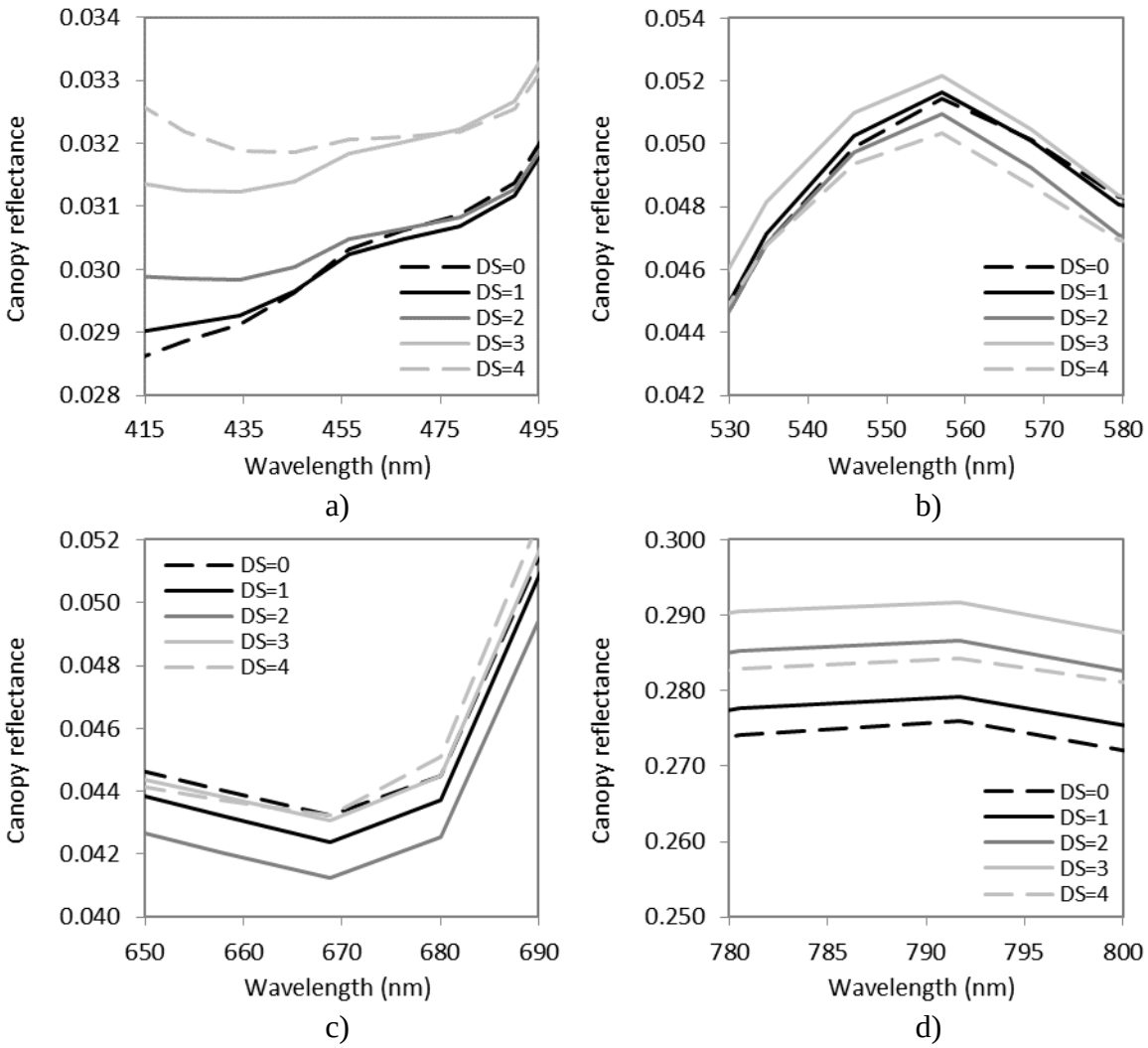

Figure 10. Mean canopy reflectance of asymptomatic and *Xf-infected* trees extracted from the airborne hyperspectral images, showing the spectral differences in the blue (a), green (b), red (c), and near-infrared (d) regions.

The PRI_n (Figure 11a), PRI×CI (Figure 11b), normalized phaeophytinization index (NPQI) (Figure 11c), and the fluorescence curvature index (CUR) (Figure 11d) indices calculated from the hyperspectral images showed trends that enabled the separation of asymptomatic and symptomatic *Xf*-infected trees (a selection of indices are shown in Figure 11). Of particular relevance were the differences observed between the asymptomatic trees (DS = 0)

and those at the early stages of infection (DS = 1), for which these indices showed statistically significant differences ($P < 0.001$).

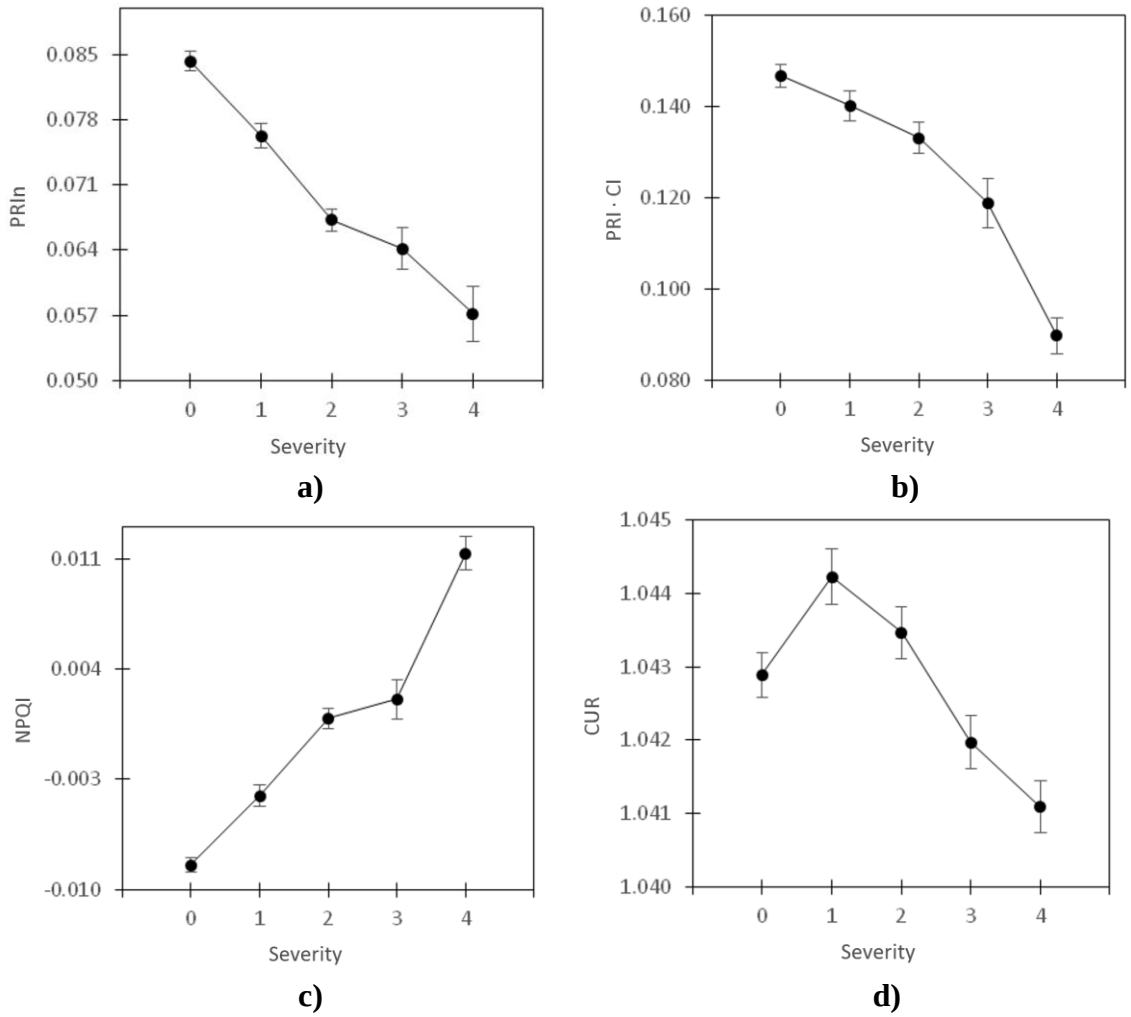

Figure 11. Mean values for the canopy-level indices PRI_n (a), PRI×CI (b), NPQI (c), and CUR (d) extracted from the airborne imagery from trees evaluated as having disease severity levels ranging from 0 to 4. The error bars represent the standard error.

Using PROSAIL, model inversions of the pure vegetation pixels extracted from the hyperspectral images were found to fit the different DS levels (Figure 12). These inversions were used to retrieve the leaf parameters Cab, carotenoids (Car), and Anth; the structural parameters LAI and the leaf inclinations distribution function (LIDF); and to quantify the fluorescence using a 3D model FluorFLIGHT (Hernandez-Clemente *et al.*, 2017; see Zarco-Tejada *et al.*, 2018 for the full description of the inversion methods used). These estimated plant traits, along with the spectral indices, CWSI, SIF, and the single spectral reflectance bands, enabled the assessment of the machine-learning methods using a reduced number of bands and spectral indices. This approach allowed us to assess the impact of the thermal indicators (CWSI) and fluorescence (SIF) for the large-scale remote sensing monitoring of *Xf* infection.

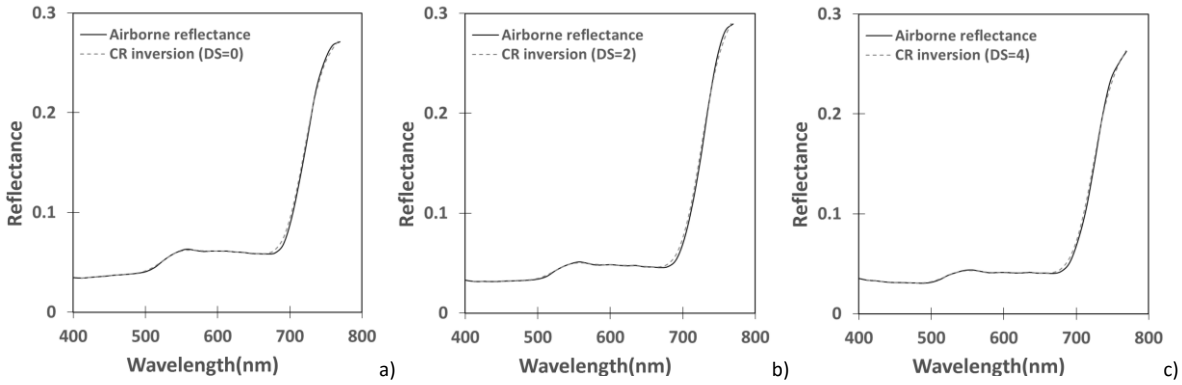

Figure 12. Reflectance spectra of individual tree crowns extracted from the hyperspectral imagery for different *Xf* disease severity levels (asymptomatic, moderate, advanced) and the corresponding fitted spectra derived from the inversion of PROSAIL.

Support vector machines using a fine Gaussian (radial basis) function were able to most accurately distinguish between asymptomatic and *Xf*-symptomatic trees, and had the smallest standard deviation among all iterations (s.d. = 0.1). In the case of the decision trees, the most accurate algorithm (73%; $\kappa = 0.23$) was the tree with the lowest number of splits. Subdividing the datasets randomly did not have a relevant impact on the decision trees. In addition, when RUSBoost trees were used, the accuracy only increased by 0.5%. As boosting functions tend to improve the classification when unbalanced data are used (Galar *et al.*, 2011), the limited improvement observed in this study could be explained by the fact that the training data contained equal numbers of asymptomatic and symptomatic cases. When comparing the accuracy of the ANN models, the variation differed by only 0.2% on average between the training algorithms using five or 10 nodes integrating the hidden layer, with the training algorithm with five hidden nodes presenting the highest accuracy. The SVM using the finest Gaussian function (with a kernel scale of 0.56) was the most accurate algorithm (with an overall accuracy (OA) of ~80% and $\kappa = 0.42$), and was therefore selected to model the asymptomatic *vs*. *Xf*-symptomatic classes using the convoluted bandsets and the pool of indices as inputs.

The SVM models with 300 iterations using information from the CIR and RGB bandsets had accuracies ranging from 63.0% to 66.7%, with κ values of 0.17 and 0.25, respectively. The highest accuracy was reached when RGB values were combined with CWSI and SIF in the model (Table 1). The RGB bandset reached higher levels of accuracy in all combinations when compared with the NGR bandset. In both cases, the inclusion of either CWSI or SIF improved the accuracy of the prediction by around 2–3%. The effect of including both SIF and CWSI was higher than adding them independently, yielding increments of 5% OA. These

results indicate that, when acquiring imagery with RGB or CIR cameras, the overall accuracy for detecting *Xf*-infected trees decreased from 80% and κ = 0.42 when using all plant traits, NBHIs, CWSI, and SIF (Zarco-Tejada *et al*., 2018) to 63% and a very poor κ = 0.17 when using CIR alone and 67% and κ = 0.25 when using the RGB data alone. The combination of both thermal (CWSI) and fluorescence (SIF) traits increased the accuracy to over 70% and κ = 0.3 when an RGB camera was used.

Table 1. Overall accuracy (OA; %) and kappa coefficient (κ) obtained when classifying symptomatic *vs*. asymptomatic trees using the near-infrared (NIR), green (G), and red (R) bands (CIR bandset), and the red (R), green (G), and blue (B) bands (RGB bandset) when combined with the Crop Water Stress Index (CWSI) and solar-induced fluorescence (SIF) traits. The SVM algorithm was used to classify the asymptomatic and *Xf*-symptomatic trees.

Inputs	Inputs (OA %)	Inputs+CWSI (OA %)	Inputs+SIF (OA %)	Inputs+CWSI+SIF (OA %)
CIR	63.0 ± 1 (κ=0.17)	65.0 ± 1 (κ=0.23)	66.0 ± 1 (κ=0.23)	68.4 ± 1.1 (κ=0.3)
RGB	66.7 ± 1.3 (κ=0.25)	68.7 ± 1.1 (κ=0.25)	68.0 ± 0.9 (κ=0.28)	71.2 ± 0.9 (κ=0.3)

R = 670 nm (full-width half-maximum, FWHM = 100 nm); G = 550 nm (FWHM = 100 nm); B = 450 nm (FWHM = 50 nm); NIR = 800 nm (FWHM = 50 nm).

The 35 spectral bands generated by convoluting the spectra were sorted based on their collinearity using a VIF analysis, then included one by one in the models. The VIF analysis organized the bands from the least collinear ones (containing the most unique information) to those with the highest collinearity (most redundant). The order of the accuracy achieved using the function of the included bands resulting from the VIF analysis is shown in Figure 13. The results obtained as a benchmark (PSFT) and those obtained using the CIR camera are shown as a reference.

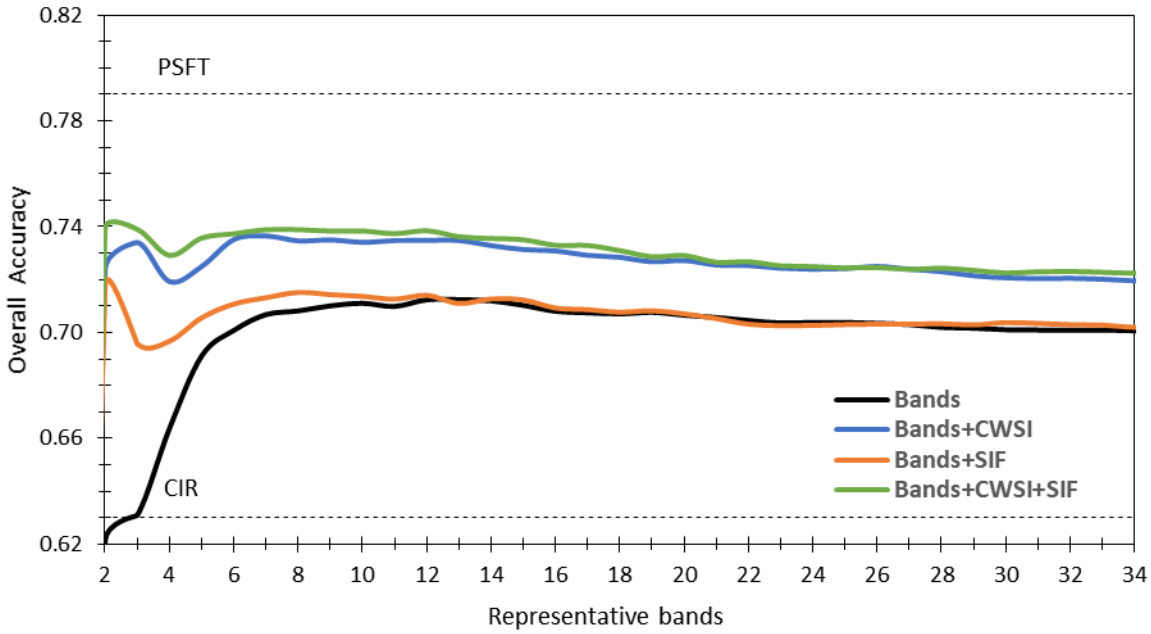

Figure 13. Overall accuracy (OA; %) reached when classifying asymptomatic *vs*. *Xf*-symptomatic trees using 35 narrow spectral bands sorted based on a variance inflation factor (VIF) analysis as inputs, either alone or combined with solar-induced fluorescence (SIF) and crop water stress indicator (CWSI) scores. The representative VIF-based bands selection was: 400, 669, 760, 714, 423, 535, 479, 736, 602, 769, 445, 412, 691, 434, 781, 512, 725, 457, 557, 747, 702, 468, 501, 624, 490, 524, 568, 546, 646, 579, 680, 591, 658, 613, and 635 nm.

When CWSI and SIF were not included in the model, at least 10 bands had to be included to reach an OA of 70%. A model built using only the first two significant bands resulting from the VIF analysis showed the lowest accuracy (OA = 62% and κ = 0.16), even lower than the model using only the CIR bandset as an input (OA = 63% and κ = 0.17). For the first six bands, the addition of individual bands into the model resulted in a proportional increase in accuracy; however, this increase was not observed when the seventh spectral band was added. The addition of SIF and CWSI together increased the accuracy of any otherwise pure band model. Moreover, the combination of bands and CWSI was found to be critical: the greatest effect was reached when CWSI was included as an input, yielding the highest accuracy (OA

~74% and κ = 0.36) when included either alone or in combination with SIF. The same approach used for the NBHIs as inputs in the SVM algorithms was taken with 11 indices selected based on the VIF analysis, after which CWSI and SIF were again included to assess the performance of the models. The most representative indices (least collinear) emerging from the VIF analysis were VOG2, TCARI/OSAVI, NPQI, DCabCxc, CRI_{700M}, modified PRI (PRI_{M1}), PRI_{M4}, PRI_n, PRI×CI, blue-fluorescence index (BF1), and CUR.

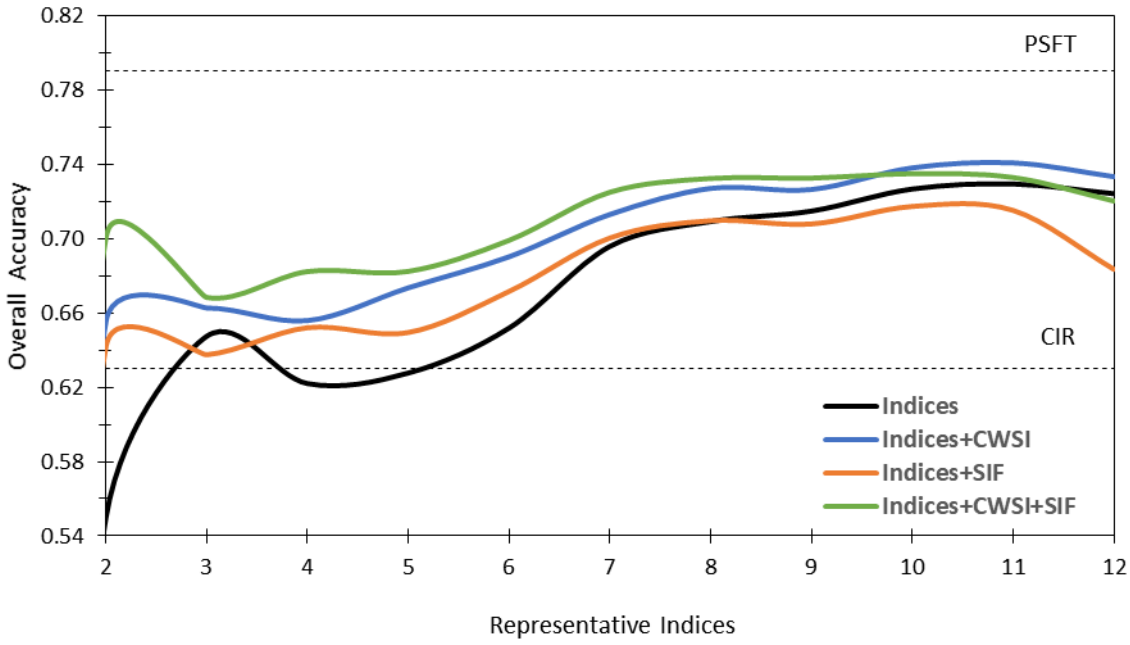

Figure 14. Overall accuracy obtained when classifying symptomatic *vs*. asymptomatic trees using 11 narrow-band hyperspectral indices as inputs, sorted based on a variance inflation factor (VIF) analysis, and combined with SIF and CWSI. The representative VIF-based index selection sorting was as follows: VOG2, TCARI/OSAVI, NPQI, DCabCxc, CRI_{700M}, PRI_{M1}, PRI_{M4}, PRI_n, PRI×CI, BF1, and CUR.

Models that used only spectral indices showed a lower accuracy compared with the models that also included SIF and CWSI information (Figure 14). The SVM using only the first two indices had an accuracy of 55%, which was the lowest accuracy in this study obtained using

SVM modeling. Contrary to the results obtained in the analysis using the bands as inputs, the 'plateau' in accuracy was reached in the model built using the first nine VIF-selected indices. After that, the accuracy increase obtained by including the CWSI and SIF information was only 1%. This result suggests that, when including the ninth least collinear index, extra information such as CWSI and SIF did not impact the asymptomatic *vs*. *Xf*-symptomatic classification.

Using a receiving operating characteristics (ROC) analysis, the relative contribution of each input to the detection of *Xf* infection was quantified for each set of inputs as follows: i) spectral bands, considering the 10 most representative bands (Figure 15a); ii) multispectral indices, considering the 10 most representative indices (Figure 15b); iii) plant traits estimated using the model inversion (Figure 15c); and iv) the PSFT model used as a benchmark (Figure 15d). These inputs were evaluated and ranked based on their importance in each model. The most relevant spectral bands that could be used to distinguish the asymptomatic and *Xf*-symptomatic trees were the 400-nm and 423-nm bands (blue region), representing over 0.65 of the importance. This result is consistent with the index NPQI being one of the most sensitive indices for the detection of *Xf* infection shown in Zarco-Tejada *et al.* (2018). By contrast, the lowest level of importance was obtained for bands beyond 735 nm (near-infrared region) that were included in the model, with an importance below 0.5. Regarding the indices (Figure 15b), the ones with high impacts on the accuracy of the SVM models were NPQI, PRI×CI, and PRI_n. Finally, CWSI had a higher impact than SIF on all models tested, which was consistent with the results shown previously (Figure 13).

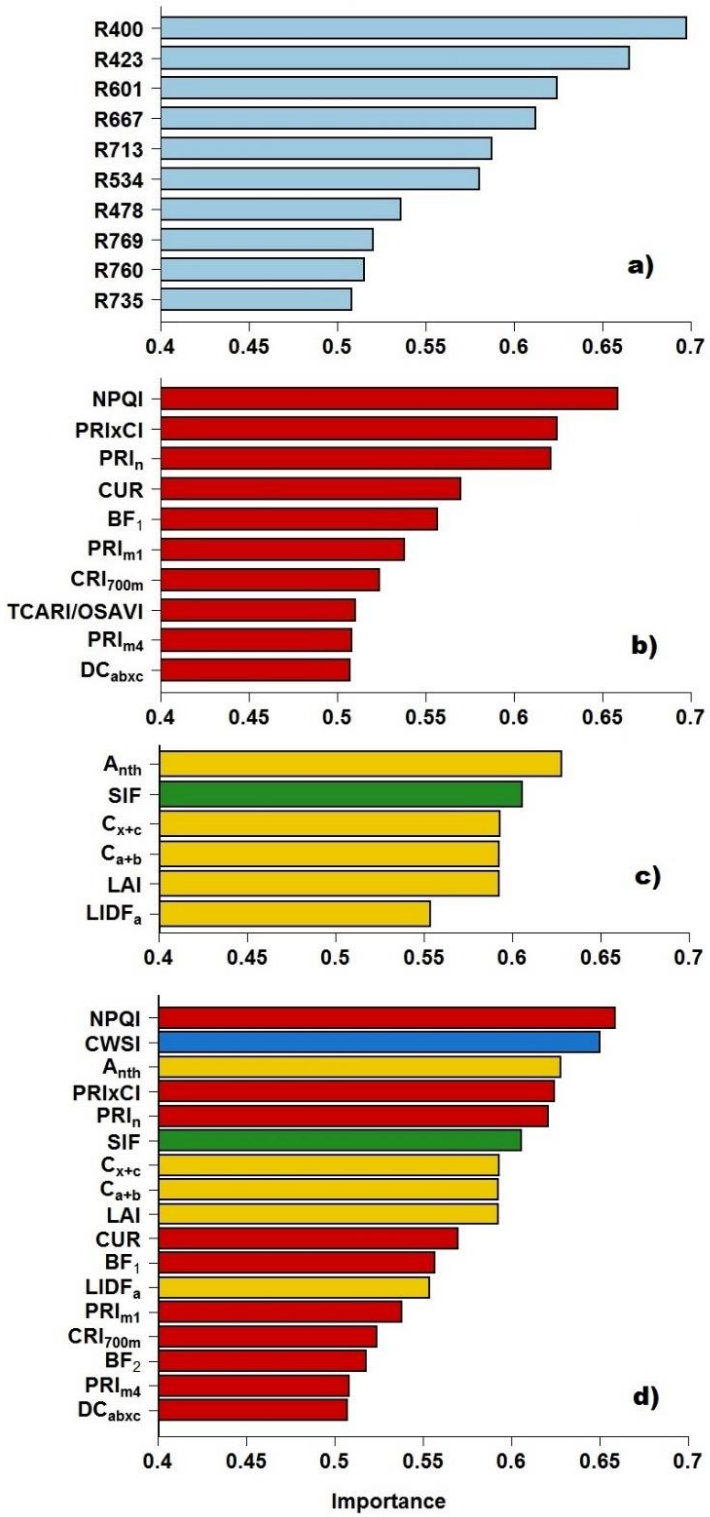

Figure 15. ROC analysis (training dataset, TR 80% 2016+2017; testing dataset, TS 20% 2016+2017) from the pool of spectral bands (a), multispectral indices (MI) (b), RT-inverted plant traits (c), and pigment-, structural-, fluorescence-, and tree temperature-based plant functional traits (PSFTs) (d) for the identification of asymptomatic *vs*. *Xf*-symptomatic trees using airborne hyperspectral imagery.

These results demonstrate that large-scale monitoring of infected areas using cost-efficient multispectral cameras built with user-selectable bands on board manned and unmanned aerial platforms is feasible. Nevertheless, careful selection of the spectral bands is critical, and it should be based on the sensitivity of specific spectral regions to the *Xf*-induced symptoms (as shown in Figure 15). Standard RGB and CIR cameras would yield very low performance, as demonstrated in this study by very low *kappa* coefficients (Table 1). The best camera configuration for the *Xf* detection, defined by six to 12 narrow spectral bands in addition to the thermal region, makes difficult to scale up these methods to current satellite sensors. The three main reasons rely on i) the spatial resolution required to target pure tree crowns in heterogeneous orchards (i.e. usually requiring submeter resolution, ideally under 60 cm pixel size); ii) the need for spectral bands located in specific regions as shown in this study, particularly the blue region; and iii) the need for high-resolution thermal images to derive tree temperature and thermal indicators such as CWSI from pure vegetation pixels. These three aspects are critical when attempting to detect early symptoms of the disease, the most important stage to successfully eradicate and to prevent the spread of *Xf* to other areas (Almeida, 2016).

When the objective is to detect the damage caused by the disease over large areas, structural symptoms such as tree crown defoliation and identification of dead trees become more straight forward through standard remote sensing indices such NDVI. In such case, scalability of these methods has been proved successful using Sentinel-2 imagery (Hornero *et al.,* 2020), demonstrating that the temporal variation of the Atmospherically Resistant Vegetation Index (ARVI) and the Optimized Soil-Adjusted Vegetation Index (OSAVI) tracked the temporal increase in disease severity and incidence. Nevertheless, due to the

lower spatial resolution (10, 20 and 60 m for the case of Sentinel-2) the use of physical models was required to understand the large effects caused by the seasonal variation of the understory in this type of orchards. Although the temporal domain is critical to understand the spread of the disease, monitoring *Xf* over permanent crops does not impose heavy requirements regarding the revisit times needed. In fact, it has been reported that plants infected with *Xf* take 10 to 12 months to develop visible symptoms (Almeida, 2016; Saponari *et al.*, 2016). Thus, in such context of permanent crops, the spectral and spatial characteristics become more critical than the temporal domain when aiming at its early detection.

The work presented here relied on a multi-year database collected over one *Xf* infected region in Southern Italy. Although results were robust due to the large number of trees evaluated over two years (Zarco-Tejada *et al.*, 2018), additional data are needed to assess the applicability of these results to other olive regions affected by *Xf*, but more importantly to evaluate the validity of the algorithms to other species affected by *Xf*. From the physiological point of view, it is expected that the spectral plant traits sensitive to the *Xf* in olive will differ in other species. Future work will evaluate the relative importance of the spectral plant traits identified in olive for the case of almond trees and other species already infected in Europe. In addition, methods to successfully differentiate biotic from abiotic stress will be needed for the operational detection of *Xf* and other harmful diseases worldwide.

4. Conclusions

The use of leaf measurements and canopy-level spectra has consistently demonstrated that blue reflectance is highly affected by *Xf*-induced stress, particularly between the wavelengths

of 400 and 450 nm. At the leaf level, spectra measured from symptomatic and asymptomatic leaves sampled from *Xf*-infected trees showed trends in their blue reflectance consistent with the DS level of the tree itself. These results demonstrated the importance of assessing the within-crown heterogeneity in trees infected by *Xf*, as the leaves sampled from infected trees showed a large spectral gradient as a function of severity. In such contexts, very high spatial resolution is crucial for the pre-visual detection of *Xf*-induced plant diseases.

The best results obtained for the detection of *Xf* infection using hyperspectral imagery and plant-trait retrievals through the physical model inversion (PSFT) decreased from ~80% (when using the full hyperspectral dataset, used here as benchmark) to ~67% and ~63% overall accuracies (and kappa, κ below 0.25) when only the RGB and CIR spectral bands, respectively, were simulated as inputs in a machine learning SVM Gaussian model. When 10-nm FWHM spectral bandsets simulating commercial multispectral cameras were used in the analyses, the use of six bands without thermal data resulted in an accuracy lower than 70%, whereas when information from the six bands was coupled with the thermal data, the model was predicted to yield up to a ~74% OA (κ=0.36). If thermal information was already included, the increase in performance was marginal when adding SIF. This highlighted the importance of coupling the thermal region with the multispectral information for the most accurate detection of *Xf* infection. Among the spectral indices assessed, those related to pigment degradation in the blue region (NPQI, bands 415 and 435 nm), the carotenoid and xanthophyll pigment indices DCabCxc (bands 672, 550 and 708 nm), CRI_{700M} (bands 515 and 700 nm), PRI_{M1} (bands 512 and 531 nm), PRI_{M4} (bands 531, 570 and 670 nm), PRI_n (bands 531, 570, 670, 700 and 800 nm), PRI×CI (bands 531, 570, 700 and 760 nm), and

chlorophyll indices VOG2 (bands 715, 726, 734 and 747 nm), TCARI/OSAVI (bands 550, 670, 700 and 800 nm) coupled with thermal (CWSI) resulted in the highest accuracy (~73%), which was not increased when more indices were added. Results showed in this study demonstrate that multispectral and thermal cameras can be used for large-scale monitoring of *Xylella fastidiosa* infected areas as long as the bandsets are carefully selected based on the sensitivity of the spectral bands to the physiological changes occurring to infected vegetation.

Acknowledgments

Data collection was partially supported by the European Union's Horizon 2020 research and innovation program through grants to the POnTE (Pest Organisms threatening Europe; grant 635646 from European Union's Horizon 2020 Framework Research Programme) and XF-ACTORS (*Xylella fastidiosa* Active Containment Through a Multidisciplinary-Oriented Research Strategy; grant 727987 from European Union's Horizon 2020 Framework Research Programme) projects. A. Hornero was supported by a research fellowship DTC GEO 29 "Detection of global photosynthesis and forest health from space" from the Science Doctoral Training Centre (Swansea University, UK). The authors would also like to thank D. Notario, A. Vera, and R. Romero from QuantaLab-IAS-CSIC (Spain) for their laboratory assistance and support during the airborne campaigns and image processing. B. Landa, M. Montes-Borrego, J.L. Trapero-Casas, M. Morelli, and L. Susca are acknowledged for their support during the field campaigns, as well as IPSP-CNR and the Dipartimento di Scienze del Suolo (Università di Bari, Italy) as host institutions. Any views expressed are purely those of the authors and may not, in any circumstances, be regarded as stating an official position of the European Commission.

References

Aasen, H., Honkavaara, E., Lucieer, A., and Zarco-Tejada, P.J. (2018), Quantitative Remote Sensing at Ultra-High Resolution with UAV Spectroscopy: A Review of Sensor Technology, Measurement Procedures, and Data Correction Workflows, Remote Sensing, 10, 1091; doi:10.3390/rs10071091.

Almeida, R.P.P., 2016. ECOLOGY. Can Apulia's olive trees be saved? Science 353, 346–348. https://doi.org/10.1126/science.aaf9710

Barnes, J. D., Balaguer, L., Manrique, E., Elvira, S. & Davison, A. W. (1992), A reappraisal of the use of DMSO for the extraction and determination of chlorophylls *a* and *b* in lichens and higher plants. Environ. Exp. Bot. 32, 85–100.

Berni, J.A.J., Zarco-Tejada, P.J., Suarez, L., Fereres, E. (2009), Thermal and Narrow-band Multispectral Remote Sensing for Vegetation Monitoring from an Unmanned Aerial Vehicle, IEEE Transactions on Geoscience and Remote Sensing, 47, (3), 722-738.

Breiman, L. (2001) Random forests. Machine learning, 45, 5-32.

Breslow, L. A. & D. W. Aha (1997) Simplifying decision trees: A survey. The Knowledge Engineering Review, 12, 1-40.

Blackburn, G. A. (2006). Hyperspectral remote sensing of plant pigments. Journal of experimental botany, 58(4), 855-867.

Calderón, R., Navas-Cortés, J.A., Lucena, C., Zarco-Tejada, P.J. (2013). High-resolution airborne hyperspectral and thermal imagery for early detection of Verticillium wilt of olive using fluorescence, temperature and narrow-band spectral indices. Remote Sens. Environ. 139, 231–245. https://doi.org/10.1016/j.rse.2013.07.031

Deng, L., Z. Mao, X. Li, Z. Hu, F. Duan & Y. Yan (2018) UAV-based multispectral remote sensing for precision agriculture: A comparison between different cameras. ISPRS journal of photogrammetry and remote sensing, 146, 124-136.

Dreiseitl, S. & L. Ohno-Machado (2002) Logistic regression and artificial neural network classification models: a methodology review. Journal of biomedical informatics, 35, 352-359.

EFSA, 2018. Updated pest categorisation of *Xylella fastidiosa*. EFSA J. 16, e05357. https://doi.org/10.2903/j.efsa.2018.5357.

EPPO, 2019. First report of *Xylella fastidiosa* in Israel. EPPO Reporting Service no. 6, article 2019/121.

Feret, J.-B., Gitelson, A., Noble, S.D., Jacquemoud, S. (2017). PROSPECT-D: Towards modeling leaf optical properties through a complete lifecycle. Remote Sens. Environ. 193, 204–215. https://doi.org/10.1016/j.rse.2017.03.004

Galar, M., A. Fernandez, E. Barrenechea, H. Bustince & F. Herrera (2011) A review on ensembles for the class imbalance problem: bagging-, boosting-, and hybrid-based approaches. IEEE Transactions on Systems, Man, and Cybernetics, Part C (Applications and Reviews), 42, 463-484.

Gamon, J., J. Penuelas & C. Field (1992) A narrow-waveband spectral index that tracks diurnal changes in photosynthetic efficiency. Remote Sensing of environment, 41, 35-44.

Gastellu-Etchegorry, J. P., Demarez, V., Pinel, V., & Zagolski, F. (1996). Modeling radiative transfer in heterogeneous 3-D vegetation canopies. Remote Sensing of Environment, 58,131–156.

Gastellu-Etchegorry, J. P., Martin, E., & Gascon, F. (2004). DART: A 3D model for simulating satellite images and studying surface radiation budget. Internation Journal of Remote Sensing, 25,73–96.

Haboudane, D., J. R. Miller, N. Tremblay, P. J. Zarco-Tejada & L. Dextraze (2002) Integrated narrow-band vegetation indices for prediction of crop chlorophyll content for application to precision agriculture. Remote sensing of environment, 81, 416-426.

Hernández-Clemente, R., North, P. R., Hornero, A., & Zarco-Tejada, P. J. (2017). Assessing the effects of forest health on sun-induced chlorophyll fluorescence using the FluorFLIGHT 3-D radiative transfer model to account for forest structure. Remote Sensing of Environment, 193, 165-179.

Homolova, L., Malenovský, Z., Clevers, J. G., García-Santos, G., & Schaepman, M. E. (2013). Review of optical-based remote sensing for plant trait mapping. Ecological Complexity, 15, 1-16.4.

Hornero, A., Hernández-Clemente, R., North, P.R.J., Beck, P.S.A., Boscia, D., Navas-Cortes, J.A., Zarco-Tejada, P.J. (2020), Monitoring Xylella fastidiosa infection symptoms in olive orchards using Sentinel 2 imagery and 3-D radiative transfer modelling, Remote Sensing of Environment, 236, 111480.

Houborg, R., Fisher, J. B., & Skidmore, A. K. (2015). Advances in remote sensing of vegetation function and traits.

Hsu, C.-W., C.-C. Chang & C.-J. Lin (2003) A practical guide to support vector classification.

Jacquemoud, S., & Baret, F. (1990). PROSPECT: A model of leaf optical properties spectra. Remote Sensing of Environment,34,75−91.

Jackson, R. D., S. Idso, R. Reginato & P. Pinter (1981) Canopy temperature as a crop water stress indicator. Water resources research, 17, 1133-1138.

Jhan, J.-P., J.-Y. Rau & C.-Y. Huang (2016) Band-to-band registration and ortho-rectification of multilens/multispectral imagery: A case study of MiniMCA-12 acquired by a fixed-wing UAS. ISPRS Journal of Photogrammetry and Remote Sensing, 114, 66-77.

Kattenborn, T., Fassnacht, F. E., & Schmidtlein, S. (2019). Differentiating plant functional types using reflectance: which traits make the difference? Remote Sensing in Ecology and Conservation, 5(1), 5-19.

Li, P., & Wang, Q. (2011). Retrieval of leaf biochemical parameters using PROSPECT inversion: A new approach for alleviating ill-posed problems. IEEE Transactions on Geoscience and Remote Sensing, 49(7), 2499-2506.

McLachlan, G. 2004. Discriminant analysis and statistical pattern recognition. John Wiley & Sons.

North, P. (1996). Three-dimensional forest light interaction model using a Monte Carlo method. IEEE Trans. Geosci. Remote Sens. 34: 946–956. http://dx.doi.org/10.1109/36.508411.

Niblack, W. 1986. An introduction to digital image processing. Prentice-Hall Englewood Cliffs.

Ollinger, S. V. (2011). Sources of variability in canopy reflectance and the convergent properties of plants. New Phytologist, 189(2), 375-394.

Peñuelas, J., Filella, I., LLoret, P., Muñoz, F., Vilajeliu, M. (1995), Reflectance assessment of mite effects on apple trees. Int.J.Remote Sen. 16, 2727-2733.

Peterson, L. E. (2009) K-nearest neighbor. Scholarpedia, 4, 1883.

Purcell, A.H., 1997. *Xylella fastidiosa*, a regional problem or a global threat? J. Plant Pathol. 79, 99–105.

Plascyk, J. A. & F. C. Gabriel (1975) The Fraunhofer line discriminator MKII-an airborne instrument for precise and standardized ecological luminescence measurement. IEEE Transactions on Instrumentation and measurement, 24, 306-313.

Saponari, M., Boscia, D., Altamura, G., D'Attoma, G., Cavalieri, V., Zicca, S., Morelli, M., Tavano, D., Loconsole, G., Susca, L., Potere, O., Savino, V., Martelli, G.P., Palmisano, F., Dongiovanni, C., Saponari, A., Fumarola, G., Carolo, M.D., 2016. Pilot project on Xylella fastidiosa to reduce risk assessment uncertainties. EFSA Support. Publ. 13, n/a-n/a. https://doi.org/10.2903/sp.efsa.2016.EN-1013.

Saponari, M., Giampetruzzi, A., Loconsole, G., Boscia, D., & Saldarelli, P. (2018). Xylella fastidiosa in olive in Apulia: Where we stand. Phytopathology, 109(2), 175-186.

Sauvola, J. & M. Pietikäinen (2000) Adaptive document image binarization. Pattern recognition, 33, 225-236.

Sepulcre-Cantó, G., Zarco-Tejada, P.J., Jiménez-Muñoz, J.C., Sobrino, J.A., de Miguel, E., Villalobos, F.J. (2006), Detection of Water Stress in an Olive Orchard with Thermal Remote Sensing Imagery, Agricultural and Forest Meteorology, 136, 31-44.

Suárez, L., Zarco-Tejada, P.J., Berni, J.A.J., González-Dugo, V., Fereres, E. (2009), Modelling PRI for Water Stress Detection using Radiative Transfer Models., Remote Sensing of Environment, 113, 730-744.

Verhoef, W. (1984). Light scattering by leaf layers with application to canopy reflectance modeling: the SAIL model. Remote Sensing of Environment, 16,125−141.

Verhoef, W., Jia, L., Xiao, Q., Su, Z. (2007). Unified Optical-Thermal Four-Stream Radiative Transfer Theory for Homogeneous Vegetation Canopies. IEEE Trans. Geosci. Remote Sens. 45, 1808–1822. https://doi.org/10.1109/TGRS.2007.895844.

Vogelmann, J., B. Rock & D. Moss (1993) Red edge spectral measurements from sugar maple leaves. Remote Sensing, 14, 1563-1575.

Zarco-Tejada, P. J., Miller, J. R., Noland, T. L., Mohammed, G. H., & Sampson, P. H. (2001). Scaling-up and model inversion methods with narrowband optical indices for chlorophyll content estimation in closed forest canopies with hyperspectral data. IEEE Transactions on Geoscience and Remote Sensing, 39(7), 1491-1507.

Zarco-Tejada, P.J., Berni, J.A.J., Suárez, L., Sepulcre-Cantó, G., Morales, F., Miller, J.R. (2009), Imaging Chlorophyll Fluorescence from an Airborne Narrow-Band Multispectral Camera for Vegetation Stress Detection, Remote Sensing of Environment, 113, 1262-1275.

Zarco-Tejada, P.J., González-Dugo, V., Berni, J.A.J. (2012), Fluorescence, temperature and narrow-band indices acquired from a UAV platform for water stress detection using a micro-hyperspectral imager and a thermal camera, Remote Sensing of Environment, 117, 322-337.

Zarco-Tejada, P.J., Camino, C., Beck, P.S.A., Calderon, R., Hornero, A., Hernández-Clemente, R., Kattenborn, T., Montes-Borrego, M., Susca, L., Morelli, M., Gonzalez-Dugo, V., North, P.R.J., Landa, B.B., Boscia, D., Saponari, M., Navas-Cortes, J.A. (2018), Pre-visual symptoms of *Xylella fastidiosa* infection revealed in spectral plant-trait alterations, Nature Plants, DOI: 10.1038/s41477-018-0189-7.